

Molecular Gas, Dust and Star Formation in the Barred Spiral NGC 5383¹

Kartik Sheth¹

Astronomy Department, University of Maryland, College Park, MD 20742-2421

Michael W. Regan^{2,3,4}

Carnegie Institution of Washington, Department of Terrestrial Magnetism, 5241 Broad Branch Road, Washington D.C. 20015

and

Stuart N. Vogel⁵, & Peter J. Teuben⁶

Astronomy Department, University of Maryland, College Park, MD 20742-2421

¹Based on observations with the NASA/ESA Hubble Space Telescope, obtained at the Space Telescope Science Institute, which is operated by the Association of Universities for Research in Astronomy, Inc. under NASA contract No. NAS5-26555.

¹E-mail: kartik@astro.umd.edu

²E-mail: mregan@dtm.ciw.edu

³Hubble Fellow

⁴Visiting Astronomer, Kitt Peak National Observatory, National Optical Astronomy Observatories, which is operated by the Association of Universities for Research in Astronomy, Inc. (AURA) under cooperative agreement with the National Science Foundation.

⁵E-mail: vogel@astro.umd.edu

⁶E-mail: teuben@astro.umd.edu

ABSTRACT

We have mapped the barred spiral NGC 5383 using the BIMA millimeter-wave array for observations of CO (J=1–0), the Palomar 1.5m for H α and optical broadband, and the Kitt Peak 1.3m for near-IR broadband. We compare the observed central gas and dust morphology to the predictions of recent hydrodynamic simulations calculated using the Piner, Stone, and Teuben code. In the nuclear region, our observations reveal three peaks lying along a S-shaped gas and dust distribution: two of these are at the inner end of offset bar dust lanes at the presumed location of the inner Lindblad resonance, and the other lies closer to the nucleus. In contrast, the model predicts a circumnuclear ring, not the observed S-shaped distribution; moreover, the predicted surface density contrast between the central gas accumulation and the bar dust lanes is an order of magnitude larger than observed.

These discrepancies remain for all our simulations which produce offset bar dust lanes, and indicate that the model is missing an essential process or component. A small nuclear bar might account for the discrepancy, but we rule this out using a HST NICMOS image: this reveals a nuclear trailing spiral, not a bar; we show that coarser resolution (i.e. ground-based images) can produce artifacts that resemble bars or rings. We conclude that the discrepancies in morphology and contrast are due to the omission of star formation from the model; this is supported by the observed high rate of central star formation ($7 M_{\odot} \text{ yr}^{-1}$), a rate that can consume most of the accumulating gas.

As is common in similar bars, the star formation rate in the bar between the bar ends and the central region is low ($0.5 M_{\odot} \text{ yr}^{-1}$), despite the high gas column density in the bar dust lanes; this is generally attributed to shear and shocks. We note a tendency for the HII regions to be associated with the spurs feeding the main bar dust lanes, but these are located on the leading side of the bar. We propose that stars form in the spurs, which provide a high column density but low shear environment. HII regions can therefore be found even on the leading side of the bar because the ionizing stars pass ballistically through the dust lane.

Subject headings: galaxies: individual (NGC 5383) — galaxies: ISM — galaxies: starburst — galaxies:structure — radio lines: galaxies

1. INTRODUCTION

Barred spirals constitute a large fraction of all disk galaxies ($\sim 75\%$ according to a near-IR survey by Mulchaey, Regan & Kundu 1997). The non-axisymmetry of a bar potential induces gas inflow which can lead to a number of dramatic evolutionary changes in a galaxy. These include large central concentrations of molecular gas (Kenney et al. 1992; 1996 and references therein; Sakamoto 1999), central starburst activity (Heller & Shlosman 1994; Phillips 1993; Garcia-Barretto et al. 1996; Ho et al. 1997), reduction of the overall chemical abundance gradient (Martin & Roy 1994; Martinet & Friedli 1997), formation of a new bulge (Norman, Sellwood & Hasan 1996), transfer of angular momentum to the halo via dynamical friction (Tremaine & Weinberg 1984; Weinberg 1985) and the destruction of the bar itself (Norman et al. 1996; Sellwood & Moore 1999).

Though a majority of these effects depend on the gas inflow, there is no consensus on the exact mechanism for the inflow. There are at least two classes of models: cloud-based/sticky particle simulations which treat the gas as a collection of discrete particles subject to “sticky” collisions (Combes & Gerin 1985) and hydrodynamic simulations which treat gas as an ideal fluid (Athanassoula 1992b and references therein; Piner, Stone & Teuben 1995, hereafter PST95). Both models form dust lanes along the leading edge of the bar, have mass inflow, and form circumnuclear rings (Combes & Gerin 1985; PST95).

The hydrodynamic models have been remarkably successful in explaining the shapes of the main bar dust lanes, the shock signature at the location of the dust lane (Athanassoula 1992), and the overall gas kinematics in the bar (RVT97). Therefore we use the framework provided by this class of models to ask two important questions: Can the nuclear gas and dust morphology in bars be explained by these models? And can the gas flow predicted by these models provide a basis for explaining the star formation activity in the bar?

To answer these questions, we use a multi-wavelength dataset for the barred spiral NGC 5383; the dataset includes maps of millimeter wave CO ($J=1-0$) emission to trace the molecular gas, $H\alpha$ emission to trace the ionized component, and broad-band optical and near-IR emission to trace the stellar distribution and dust extinction. NGC 5383 is a prototypical early Hubble type (SBb) barred spiral galaxy. The global characteristics of NGC 5383 are summarized in Table 1. NGC 5383 has been studied with optical images (Burbidge, Burbidge & Prendergast 1962; Duval & Athanassoula 1983; Elmegreen & Elmegreen 1985), long-slit spectra (Peterson et al. 1978; Duval & Athanassoula, 1983), HI interferometric observations (Sancisi, Allen & Sullivan 1979), and single-dish CO observations (Ohta, Sasaki & Saito 1986). The standard model for some of the seminal studies of gas flow in barred spirals has also used NGC 5383 as the prototype (Huntley 1978; Sanders and Tubbs 1980; Tubbs 1982; Duval & Athanassoula 1983; A92).

We first present a comparison of nuclear gas and dust morphology in NGC 5383 to the model predictions in §4.2. The gas and dust distribution is a signature of the bar induced inflow and its subsequent evolution. If the hydrodynamic model can reproduce the observations, then it may

Table 1. Properties of NGC 5383

Parameter	Value	Reference
R.A. (J2000) ^a	13 ^h 57 ^m 04 ^s .81	(1)
Dec (J2000) ^a	41 ^d 50 ^m 47 ^s .68	(1)
D ₂₅	2'.75	(2)
Major axis P.A.	85±3°	(2)
Inclination	50°	(2)
V _{sys}	2250 km s ⁻¹	(3)
V _{3K}	2428 km s ⁻¹	...
Adopted Distance	32.4 Mpc	...
Linear scale	157 pc arcsec ⁻¹	...
Bar Length	110±3''	(1)
Bar P.A.	130±4°	(1)

^aK' band peak

References. — (1) This paper (2) Duval & Athanassoula 1983 (3) Becker, White, & Helfand 1995.

be used as an adequate model for studying gas flow in the nuclear region of bars. On the other hand, even a failure of the model can refine our understanding by pointing out missing physics in the model’s assumptions. We find that while the model is consistent with the observations in some aspects, there are several striking differences between the two. Possible reasons for these discrepancies are investigated in §4.3 where we consider presence of a nuclear bar, incomplete parameter space exploration of the model, or lack of star formation processes in the model. We conclude that the latter is at least partly responsible for the discrepancies.

In §4.5, we compare the sites of star formation with the molecular gas distribution in the bar and investigate where and under what circumstances stars form in the bar. This is important because bar star formation can affect the net mass inflow. The analysis is novel because previous studies (Tubbs 1982; Athanassoula 1992b; Reynaud & Downes 1998) have only sought to explain the lack of bar star formation. We present the first explanation of how stars may be forming in the bar, between the bar ends and the circumnuclear region.

2. OBSERVATIONS AND DATA REDUCTIONS

2.1. Optical Observations

We observed NGC 5383 in a broad band ($\Delta \lambda \sim 1240 \text{ \AA}$) R-filter and a narrow band ($\Delta \lambda = 25 \text{ \AA}$) $H\alpha$ filter at the 1.5m telescope at Palomar⁸ on the night of 2 June, 1994 with a 2048×2048 CCD camera in direct imaging mode. In this mode the camera has a $12'.7$ field of view with $0''.37$ pixels. Using the R-band filter we obtained one 300 s and one 600 s exposures which were co-added to obtain a single R-band image. The $H\alpha$ image was a single 900 s exposure. The effective resolution was $1''.5$ in the R-band image and $2''.4$ in the $H\alpha$ image. For both images we divided by a normalized flat-field frame, subtracted the mean sky brightness, and removed cosmic rays using standard routines in the NOAO/IRAF⁹ software package.

We also corrected all images for atmospheric extinction. We used the standard stars BD+26.2606 and BD+17.4703 for absolute flux calibration using the absolute photometry by Oke & Gunn (1983). Finally, we registered foreground stars in each image with the Hubble Guide Star Catalog (GSC) and determined astrometric solutions for each image. The residuals in determining absolute positions are smaller than $0''.03$; however, systematic errors in the GSC prevent us from achieving an accuracy $< 1''$. We used the R-band image to subtract the underlying continuum from the $H\alpha$ image. The final continuum-subtracted $H\alpha$ line image is shown in Figure 1.

⁸Observations were made on the 60 inch telescope at Palomar Mountain, which is jointly operated by the California Institute of Technology and the Carnegie Institution of Washington.

⁹IRAF is distributed by the National Optical Astronomy Observatories, which are operated by the Association of Universities for Research in Astronomy, Inc., under cooperative agreement with the National Science Foundation

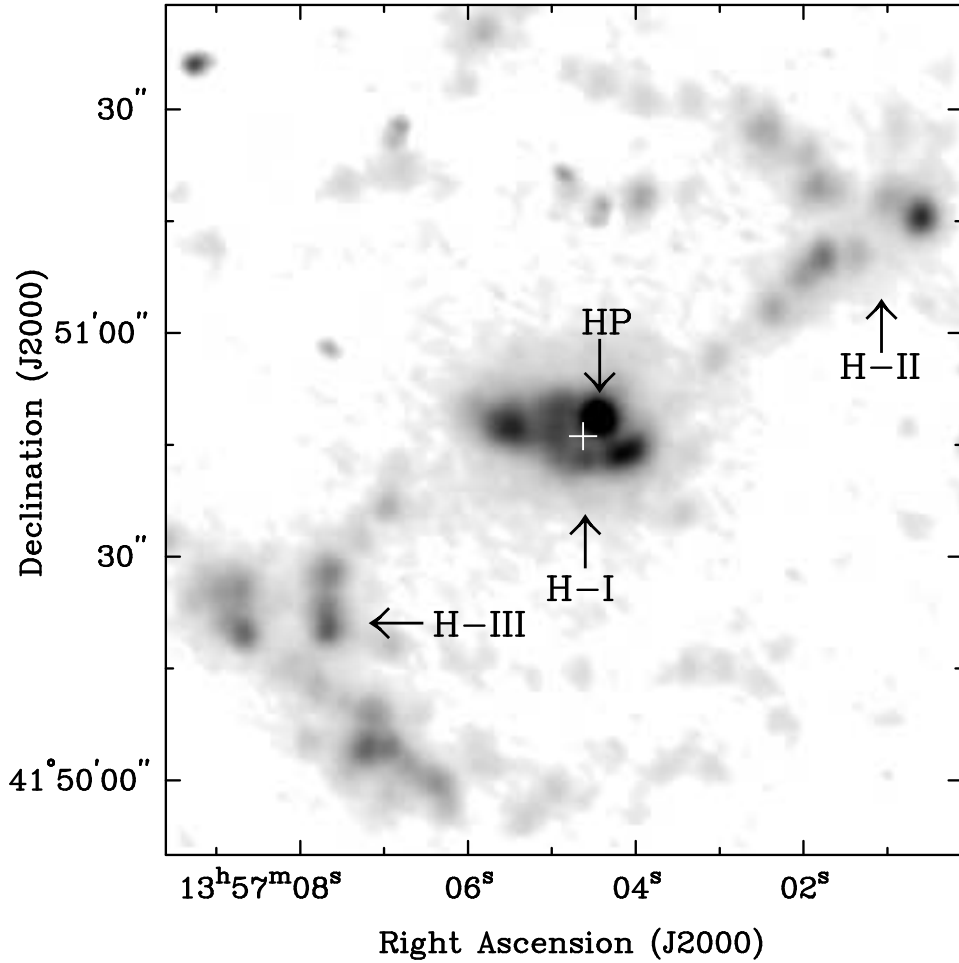


Fig. 1.— Continuum-subtracted H α image of NGC 5383 showing active star-forming regions. Note the relatively weak H α emission along much of the length of the bar compared to the strong emission in the nucleus and the bar ends. The peak H α emission is indicated by the label HP and is displaced 3".1 north northwest from the radio continuum center (indicated by the cross). The labels H-I (nuclear region), H-II (northwestern bar end + spiral arm) and H-III (southeastern bar end + spiral arm) indicate the three regions where star formation rates were calculated.

2.2. Infrared Observations

We observed NGC 5383 in the near-infrared J and K' bands (Wainscoat & Cowie 1992) on the nights of 1, 4 March 1994 at the 1.3m telescope on Kitt Peak using the Cryogenic Optical Bench (COB). The COB used a 256×256 InSb detector with 0".95 pixels ($\sim 4'$ field of view). The total on-source integration time was 24 minutes in the J band and 52 minutes in the K' band. The effective resolution is 2".4 in the K' band image and 2" in the J band image. The data were reduced via the procedure described by Regan et al. (1995). Since the K' band image traces light

primarily from the old stars which are good tracers of the gravitational potential, Figure 2 is shown to emphasize the bar potential in NGC 5383.

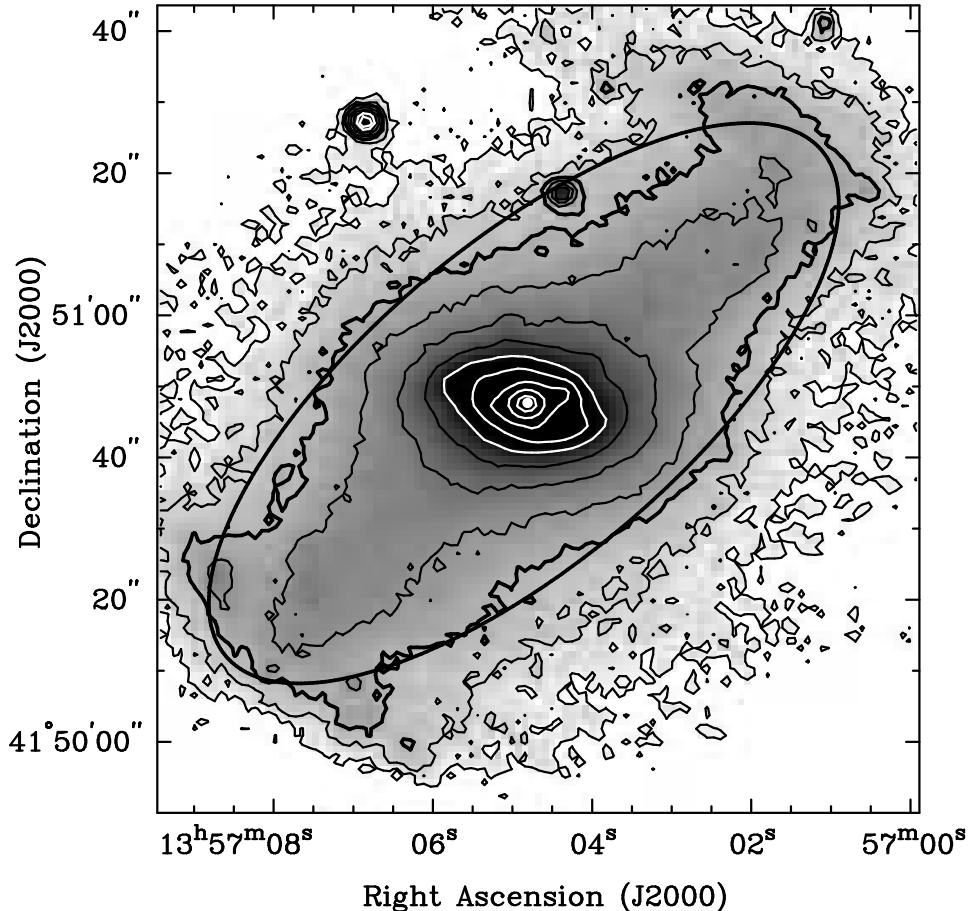


Fig. 2.— K-band ($2.25\mu\text{m}$) image of NGC 5383 tracing the old stellar population depicts the relatively smooth bar potential. The contours are at 20, 19.5, 19, and in steps of 0.5 magnitudes arcsec^{-2} thereafter. The thick ellipse is the ellipse fit with the highest ellipticity and therefore it identifies the bar. The thick contour corresponds to the mean intensity along the best-fit ellipse.

2.3. NICMOS Observations

We observed the nucleus of NGC 5383 with the F160W filter on camera 2 of the Near Infrared Camera and Multi-Object Spectrometer (NICMOS) in the Hubble Space Telescope on 13 October 1997. The F160W filter is an approximate match to ground-based near infrared H-band filters and has a central wavelength of $1.6\mu\text{m}$. Our total integration time on source was 704 seconds. The detector on Camera 2 is a 256×256 HgCdTe detector with a plate scale of 0.075 arc seconds pixel^{-1} yielding a field of view of $19''.2$. During the time period of the observations the pipeline

data reduction for NICMOS was still under development leading to output of the pipeline process that was not the best possible calibration of the data. Therefore, we re-calibrated the images using the latest flat fields, darks, and non-linearity files.

2.4. BIMA CO Interferometric Observations

We observed CO (J=1-0) line emission in NGC 5383 with the BIMA (Berkeley-Illinois-Maryland Association)¹⁰ array in three different configurations of six dishes from February-June 1994, and in a compact configuration of nine dishes from July-August 1996. The phase and pointing center for these observations was $\alpha(\text{J2000}) = 13^{\text{h}}57^{\text{m}}04^{\text{s}}.54$, $\delta(\text{J2000}) = 41^{\circ}50' 46''.00$. The correlator window was centered at $V_{\text{LSR}} = 2245 \text{ km s}^{-1}$ with a total bandwidth of 424 km s^{-1} and a resolution of 4.1 km s^{-1} . In each case the line emission was observed in the upper sideband. The projected baselines ranged from 2.2 to 87.5 k λ and the single-sideband system temperatures ranged from 500 to 1100 K. We flagged the data with anomalous visibilities resulting from shadowing of an antenna at low elevation and spurious electronic spikes (birdies and correlator window edges). The complex instrumental gain was calibrated using the quasars 1153+495, 1419+543 or 1310+323, observed every 20-30 minutes. The absolute flux calibration was determined from observations of Uranus or Mars and the structure of the IF band pass was determined from observations of the quasars 3c273 or 3c279. We imaged the calibrated data set into 10 km s^{-1} channels using natural weighting to achieve maximum signal to noise ratio and then cleaned the dirty maps using the Hogböm algorithm (Hogböm 1974). Next we employed an iterative phase-only self-calibration process (Thompson, Moran, & Swenson 1986; Regan et al. 1995) which used the CLEAN components as model inputs for the iterations. The self-calibration process did not significantly improve the results because our initial atmospheric phase calibration was good. In other words, our data are limited by thermal noise rather than the dynamic range. The synthesized beam in the maps is $4''.62 \times 4''.23$ at a position angle of 17 degrees. The final channel maps have a noise level of 50 mJy beam^{-1} . We summed over all pixels in the data cube with $|S_{\nu}| > 2\sigma$ to form a velocity-integrated total intensity map which is shown in Figure 3.

2.5. CO Single-Dish Observations

We obtained a spectrum of the center of NGC 5383 in the CO (J=1-0) emission line with the single dish, 12m NRAO¹¹ telescope on 01 December 1998. The half-power primary beamwidth of the telescope is $53''$ and the pointing accuracy is $\pm 5''$. We used the spectral line beam position

¹⁰The BIMA Array is partially funded by a grant from the National Science Foundation

¹¹The National Radio Astronomy Observatory is a facility of the National Science Foundation, operated under cooperative agreement by Associated Universities, Inc. telescope at Kitt Peak

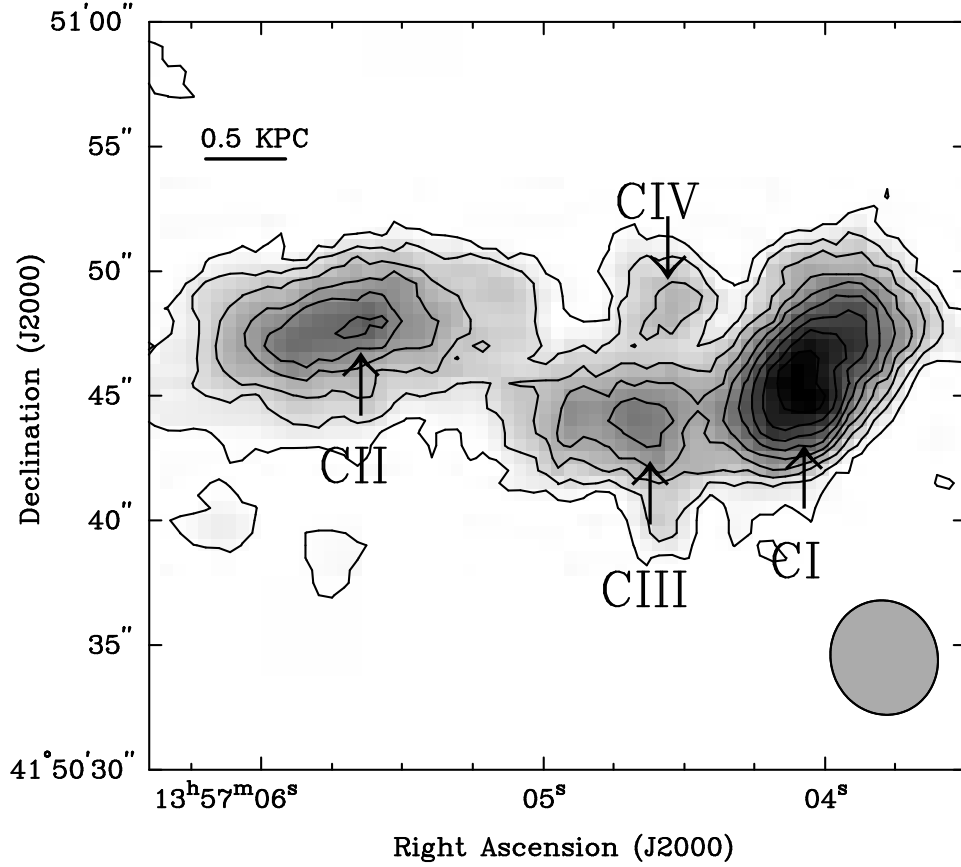


Fig. 3.— Nine-element BIMA CO (J=1-0) total intensity map, with a naturally weighted beam of $4''.62 \times 4''.23$ and contours at 2,4,6,8,10,12,14,16, and 18 σ ($1\sigma = 1.85 \text{ Jy km s}^{-1} \text{ beam}^{-1}$). CI and CII identify the “twin peaks” which coincide with the inner end of the dust lanes. CIII marks the third peak, located interior to the twin peaks. CIV is coincident with the brightest star forming region in the nucleus

switching observing mode with a $4'$ throw for the off position. The total on-source integration time was nine minutes with a system temperature of ~ 350 K. The filter banks were configured in the 2×2 MHz series mode for a total bandwidth of 512 MHz. An unstable oscillation in one channel prevented us from using data from both channels. The measured rms noise in a 2 MHz channel is 19.5 mK. A zeroth order baseline was subtracted from each of the three scans before they were co-added; the resulting spectrum is shown in Figure 4.

3. RESULTS

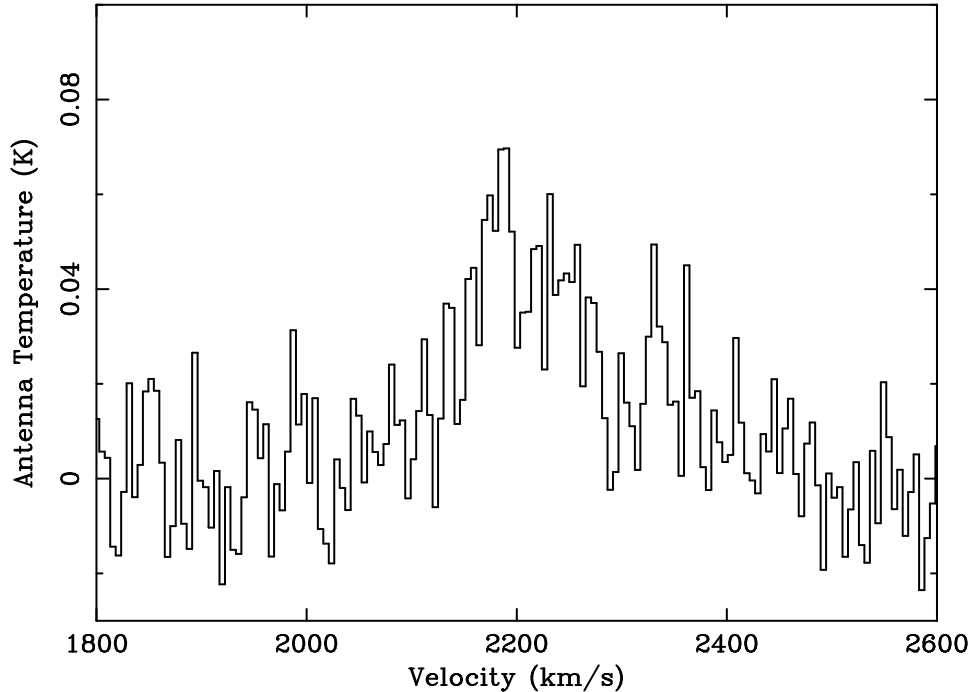


Fig. 4.— Single dish spectrum of NGC 5383 obtained with the NRAO 12m single dish telescope. Integrating from 2060 to 2430 km s⁻¹, we get a total flux of 9 K km/s.

3.1. CO Morphology

CO emission is detected in the central 3.5 kpc diameter region of the NGC 5383. We find two prominent CO peaks (labeled CI, CII in Figure 3) in the total intensity map, corresponding to the inner termini of the dust lanes¹². In addition to these two peaks, we see a third peak (labeled CIII in Figure 3) east-southeast of peak I. Peak CIII lies along the northwestern dust lane after it has curved and is heading east across the nuclear region. There is CO emission in an even weaker feature (labeled IV) 5'' north of CIII. This feature coincides with the most intense star forming region in the nucleus.

Within the primary beam (53'' FWHM) of the NRAO 12m telescope, the total CO flux in the BIMA interferometer maps is ~ 175 Jy km s⁻¹. This is about 60% of the flux (9 K km s⁻¹) measured from the NRAO spectrum, assuming a conversion factor of 33 Jy K⁻¹ for the 12m telescope. Most of the CO detected by the interferometer is concentrated in the central 35'' of NGC 5383. The CO flux in this 35'' region (165 Jy km s⁻¹) can be converted to a total H₂ mass using the standard equation $M(\text{H}_2) = 1.1 \times 10^4 D^2 S_{\text{CO}}$ (Kenney et al. 1992), where D is in Mpc

¹²In this paper, we use the term dust lane and bar dust lane interchangeably. All references to dust lanes always refer to the main bar dust lanes

and S_{CO} is in Jy km s^{-1} . For the adopted distance of 32.4 Mpc, the total molecular gas mass is $\sim 2 \times 10^9 M_{\odot}$.

3.2. Dust Extinction Morphology

We have divided the R^{13} and J band images into the K' band image to form color maps (see Figure 5).

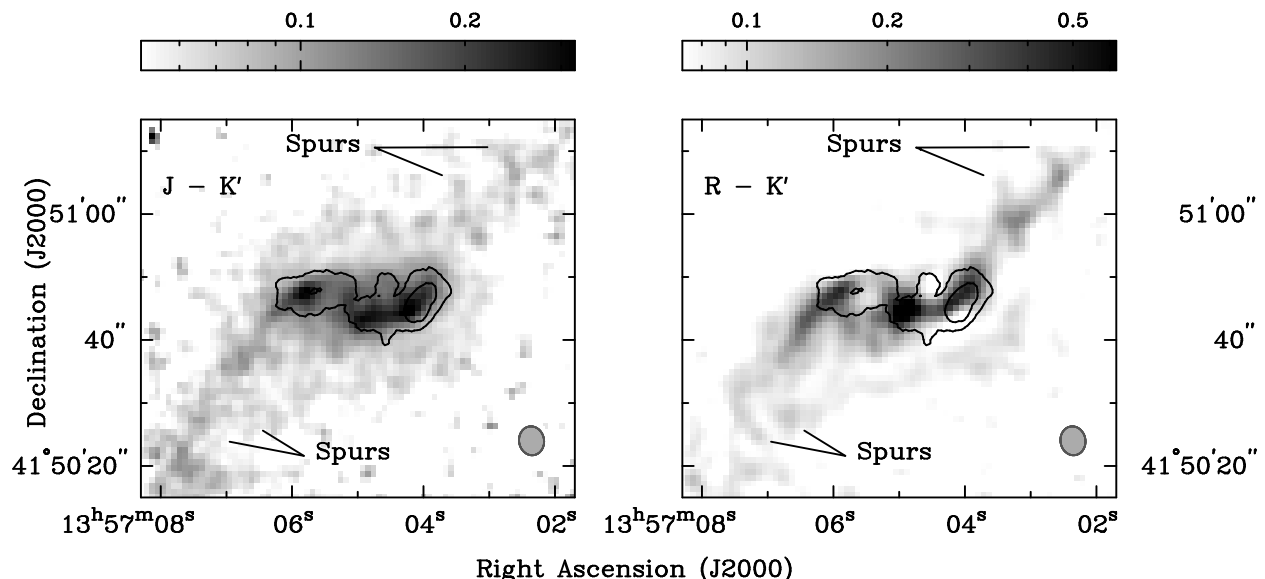


Fig. 5.— Dust extinction in NGC 5383 as traced by optical-infrared and infrared-infrared colors. The resolution of both maps is $2''.4$. Left panel: $J-K'$ color map (grey scale) of NGC 5383 tracing regions of high dust extinction. The wedge above indicates the color excess in magnitudes. Contours (4,8,12, and 16 σ) of CO (J=1-0) are overlaid to indicate the correlation between CO emission and dust extinction. The southeastern dust lane is clearly seen all the way to the bar end. The northwestern dust lane is harder to distinguish but its general structure and spurs similar to the $R-K'$ map can be seen. Right panel: $R-K'$ color map tracing regions of low dust extinction with the same CO contours as the left panel. The locations of the dust spurs are indicated in both panels.

Prior to division, the images were registered against each other and the higher resolution images were smoothed to match the lower resolution ($2''.4$) of the K' band image. In both maps

¹³We do not present the broad-band images here but we refer the reader to the paper by Burbidge et al. (1962) and the Carnegie Atlas (Sandage & Bedke, 1994) for optical images of NGC 5383. In these images, note the dust lane structure which we highlight using color maps. Also note that the spurs which are important in our discussion of bar star formation may be easier to see in these images

the darker grey scale corresponds to redder colors (higher extinction). Although it is difficult to estimate the dust content in galaxies, it has been shown that optical-infrared colors such as $R-K'$ and infrared-infrared colors such as $J-K'$ can be used to estimate the amount of dust using multiple scattering radiative transfer models (Regan et al. 1995); however, such models require images at multiple optical and infrared wavelengths to confidently parameterize the optical depth and the ratio of dust scale height relative to the stars. Even though the lack of multiple images at different wavelengths prevents us from this quantitative analysis, we can still gain a qualitative understanding of the dust distribution from the two colors available to us.

In both maps, the main bar dust lanes show up as regions of high extinction. In the $R-K'$ map, the northwestern dust lane is relatively straight and narrow with at least two spurs (indicated by arrows in Figure 5), which merge into the dust lane, and end in areas with high levels of dust extinction. In the southeastern dust lane the spurs and the dust lane are difficult to distinguish from each other, and the dust lane characteristics are harder to describe. However, this dust lane is seen more clearly in the $J-K'$ color map, where its appearance and structure is similar to the northwestern lane. Note that the northwestern dust lane, on the other hand, is not clearly visible in the $J-K'$ map. The differences between the two color maps could be due to a variety of reasons such as different dust lane thicknesses, geometry of the dust/star mixture (Witt 1992), systematic reddening of the near side of a galaxy based on its orientation in the sky (e.g. Elmegreen & Block, 1999), or the more remote possibility that the stellar populations are different between the two sides of the bar.

At the inner terminus of the dust lanes where the dust lanes begin to curve, two red peaks mark locations of the highest dust extinction. These dust extinction “twin peaks” match the peaks seen in CO emission. Interior to these peaks, a S-shaped curve is traced in dust extinction similar to the curve seen in CO emission. At the center of the S-shaped curve we find a peak with the reddest color in the map. Since this central peak coincides with the peak of K' band emission it probably reflects excess K' band emission from either a change in the underlying stellar population (excess red giant stars), or hot dust (e.g., Thatte et al. 1997; Marco & Alloin 1998), instead of a large amount of dust extinction. The S-shaped structure, the dust lanes and the spurs, however, cannot be due to K' band emission excesses because the K' band emission is much smoother (Figure 2); hence, these must be due to dust extinction.

3.3. $H\alpha$ Morphology

Strong $H\alpha$ line emission (Figure 1) is detected in the nucleus, the bar ends and the spiral arms. In the nucleus the peak $H\alpha$ emission (indicated by the label HP in Figure 1) is located $3''.1$ northwest of the radio-continuum peak¹⁴. We can clearly trace the northwestern dust lane

¹⁴Radio continuum peak position adopted from Becker, White, & Helfand (1995)

in absorption against the $H\alpha$ emission as it curves inwards, $3''$ south of HP. We also see a bright elongated HII region, $5''$ southwest of HP, along the southern edge of the dust lane. Similarly, there is another bright HII region $11''$ east of HP, near the inner terminus of the southeastern dust lane.

HII regions are also observed at both bar ends and along the spiral arms near the bar ends. Since it is unclear whether the observed HII regions belong to the bar end or the spiral arm, we use the term “bar end / spiral arm HII regions” to describe any HII regions in this area. The bar end / spiral arm HII regions mostly trail the bar, although there is at least one bright HII region on the leading side of the bar. The HII regions extend for about 4 kpc on the trailing side of the spiral arms and about half that distance along the leading side. The study of star formation activity in these regions is interesting because of the changing environment between the bar ends and spiral arms (Kenney & Lord 1991). However, in this paper, we limit the scope of our study and do not study the star formation activity in these regions.

Instead, we choose to focus on the star formation activity in the bar. While the nuclear region and the bar ends have strong $H\alpha$ emission, the bar itself is comparatively weak; this pattern is consistent with observations of other early-type barred galaxies (Garcia-Barreto et al. 1996; Koopmann & Kenney 1996; Phillips 1993). Most of this limited star formation activity in the bar of NGC 5383 is found in one or two bright star formation sites on each side of the bar, along its leading edges. These $H\alpha$ peaks are best seen in the contour image of $H\alpha$ emission in Figure 8 and their significance is discussed in §4.5.

4. DISCUSSION & ANALYSIS

4.1. Why Choose Hydrodynamic Models?

Modeling studies of gas flows in bars constitute an extensive subfield and we refer the reader to excellent reviews in Sellwood & Wilkinson (1993), Athanassoula (1992a,b), Teuben (1996) and references therein. One can broadly categorize these modeling efforts into two main categories: a) cloud-based/sticky particle simulations which treat the gas as a set of distinct particles which react to collisions based on some prescription for cloud collisions, and b) hydrodynamic (grid-based or smooth particle hydrodynamics (SPH)) simulations which treat the gas as an ideal fluid obeying the basic hydrodynamic equations. Both classes of models have advantages and disadvantages and both can provide adequate frameworks in which observations can be interpreted.

Both classes of models produce dust lanes but the hydrodynamic models alone can produce the straight dust lanes seen in strongly barred galaxies such as NGC 5383. Both classes predict gas inflow of approximately the same order of magnitude but the exact route followed by the gas is very different in each class of models. In the hydrodynamic model, the gas undergoes a shock at the dust lane and is forced to flow directly inwards in the dust lane (RVT97, Athanassoula 1992b).

In the cloud-based models, the gas clouds in the dust lane behave like those found in galaxy spiral arms. The dust lane is formed because the clouds crowd together for a longer time. However, unlike the hydrodynamic models, they eventually cross and leave the dust lane on the leading side of the bar. In this model, the clouds can collide, lose angular momentum and spiral down to the center in a few orbits (Combes & Gerin 1985).

For strong bars, the hydrodynamic model gas flow is the best match to the observed velocity fields (e.g., NGC 1530 RVT97). It is also particularly successful at producing the high shear and shock seen across the bar dust lanes (Athanasoulas 1992); these cannot be produced by the cloud-based/sticky particle models (Regan, Sheth & Vogel 1999, hereafter RSV99). Moreover, a recent study of gas kinematics in seven barred spirals also shows that the observed gas kinematics are consistent with the hydrodynamic models and not with cloud-based simulations (RSV 1999). So even though the molecular ISM is certainly not a diffuse, ideal fluid, it appears that the hydrodynamic models are better at reproducing observations than cloud-based/sticky particle models, especially for describing observations of gas kinematics and morphology in strong bars. Hence we choose to compare the CO and dust extinction morphology of NGC 5383 to a hydrodynamic model; the model chosen is the PST95 standard model.

4.2. Comparing Hydrodynamic Model Predictions to Observations

In order to compare the CO emission and dust extinction distribution to the hydrodynamic model, we projected the PST95 model (Figure 6a) to match the orientation of NGC 5383 (Figure 6b) and smoothed the model to match the resolutions of the dust extinction and CO emission maps (Figures 6c,d respectively).

The model gas distribution shows an extremely dense nuclear ring with two peaks along the ring near the bar major axis, consistent with PST95. However, we emphasize that the location of these peaks varies in the simulations. Over time additional peaks often appear and disappear in the ring, downstream of the dust lane terminus. The density contrast between the peaks and the dust lane is large; in the unsmoothed model, the peaks have a column density which is ~ 25 to 120 times higher than that in the dust lane, and the average ring column density is ~ 25 to 60 times larger. Smoothing the models reduces the average density contrast by $\sim 50\%$ at the resolution of the dust extinction maps and by $\sim 60\%$ at the resolution of the CO emission maps. We also find that the gas density in the dust lane increases inwards along the dust lanes; from the outer terminus to the inner terminus the density increases by a factor of ~ 4 . The model also produces offset bar dust lanes and an outer, low density ellipsoidal feature.

When we compare Figure 6 to Figures 3 & 5, we find significant differences between the model gas morphology and the observations. The most striking disparity is the density contrast between the dust lane gas and the ring/peak gas. The contrast in the dust extinction maps between the

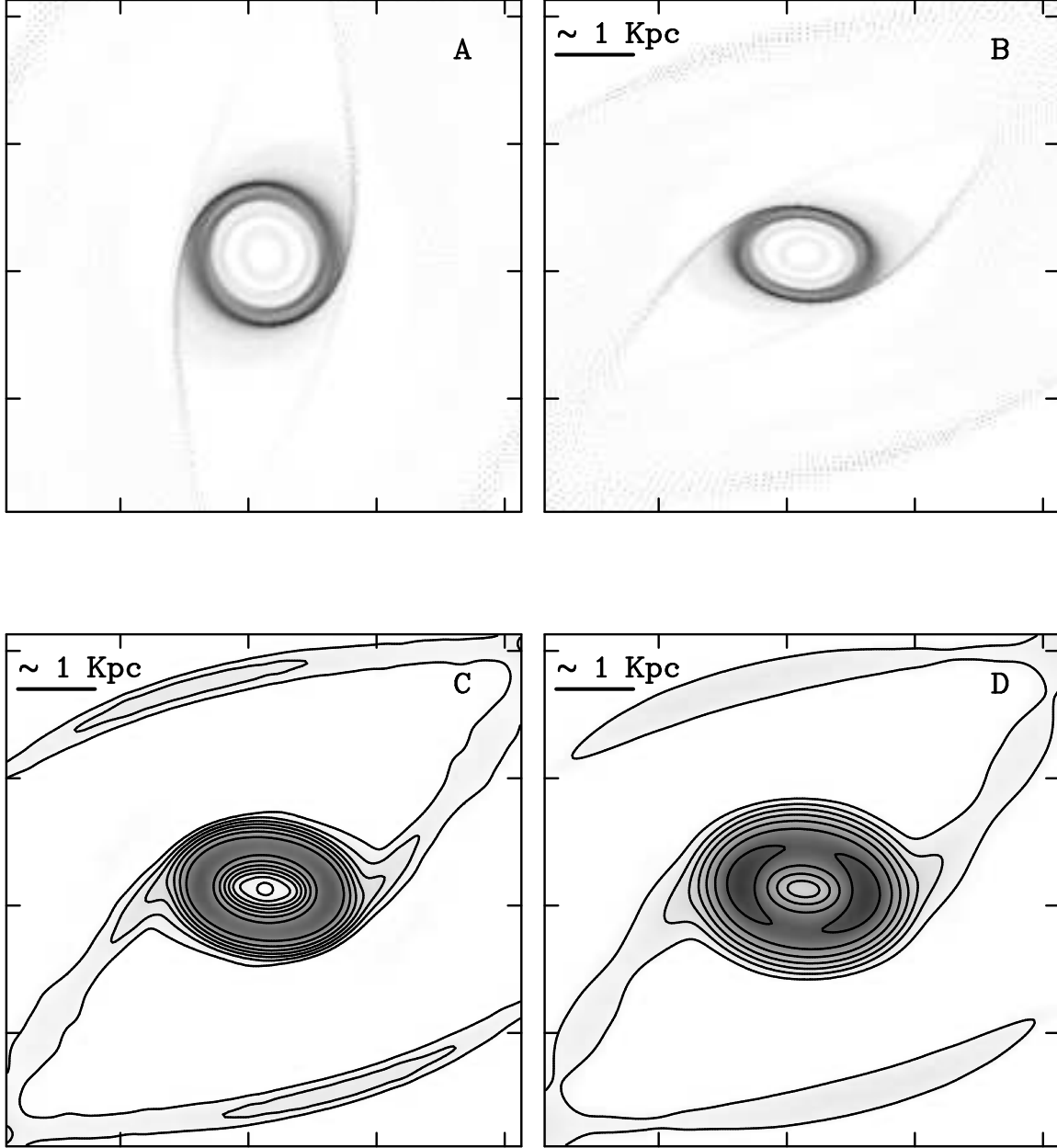


Fig. 6.— Top left: a) The PST95 hydrodynamic model. Top right: b) The model projected to match the orientation of NGC 5383. Bottom left: c) The projected model in panel (b) is smoothed to match the resolution of the dust extinction maps. Bottom right: d) The projected model smoothed to match the resolution of the CO maps. Note the increasing density inwards in the dust lane. The gas on the outside of the dust lanes (the ellipsoidal feature) connects to the bar end and remains to be studied. The contours in the smoothed models are spaced at 2, 4, 8, 16, 32, 64, 128, $256 \times$ an arbitrary density.

dust lane and the twin peaks is 1.3 in the J–K' map and 1.5 in the R–K' map¹⁵. At the same resolution, the model column density contrast is an order of magnitude ($\sim \times 8\text{--}40$) larger. Since CO is not detected in the dust lanes, only a lower limit to the CO brightness ratio between the peaks and the dust lane can be calculated. In NGC 5383, this ratio is ~ 20 , similar to that observed in NGC 3351 and NGC 6951 (Kenney et al. 1992)¹⁶. In other galaxies where CO is detected in the dust lanes (e.g. NGC 1530, see Figure 11 or Table 3 in Downes et al. 1996, or NGC 7479, see Figure 5 in Quillen et al. 1995), the CO brightness ratio between the ring/peak and the dust lane gas is only $\sim 5\text{--}10$; at the same resolution, the model density contrast is $\sim 15\text{--}70$. One reason for the high CO brightness ratio in NGC 5383 may be that the CO emissivity per H₂ molecule is enhanced in nuclear region (Regan et al. 1995) or at least at the twin peaks. Since variations in CO emissivity may determine the CO brightness ratio, dust extinction is perhaps a better tracer of the gas column density because the gas to dust ratio is better constrained than the CO to H₂ conversion factor (Sodroski et al. 1995; Regan 2000)¹⁷. Therefore comparing the dust extinction maps to the model, we conclude that the ratio of the ring to the dust lane gas surface density is an order of magnitude larger than seen in the observations.

Another striking difference between the model and the observations is the central morphology of gas and dust. In the PST95 study, a nuclear ring always formed whenever the bar had offset dust lanes (i.e. had an ILR), and whenever the bar was thick (axial ratio < 5). In NGC 5383 both of these conditions are met, yet there is no sign of a nuclear ring; instead, as described in §3.1 and §3.2, the gas and the dust are distributed in a S-shaped pattern with three peaks. In some galaxies, e.g. NGC 1530 (Regan et al. 1995), higher resolution CO maps have resolved the twin peaks structure into a broken ring or partial spiral arms. In NGC 5383, however, higher resolution uniform weighted maps (not shown) do not reveal a ring; they show the same triple peak structure seen in the lower resolution CO map. Also, the dust extinction maps, which are at a higher resolution than the CO maps, do not show a ring. In some other “twin peak” galaxies, e.g. NGC 6951, NGC 3351 and M101, a nuclear ring of HII regions has been observed (Kenney et al. 1992). However, we see no evidence of an H α ring in our data; the H α emission is amorphous and is dominated by the bright H α peak north of the nucleus (see Figure 1). While it is possible that an H α ring can be obscured by highly variable and patchy dust extinction in the nuclear region (Phillips 1993), the dust distribution in NGC 5383 is not ring-shaped and cannot hide an HII ring.

At this point, it is worthwhile to mention that the CO morphology in the center of bars can have a rich variety of morphologies in addition to “twin peaks.” As Kenney (1996) points out, there are spiral arms as in NGC 6951 (Kenney 1996), filled exponential disks as in NGC 3504

¹⁵These values are expressed as flux ratios and not magnitudes

¹⁶We assumed that the lowest contour in Figure 1 of Kenney et al. (1992) is at 2σ

¹⁷This would mean that the total molecular gas mass calculated from the standard CO to H₂ conversion factor is an upper limit

(Kenney, Carlstrom & Young 1993) or NGC 4102, and rings or partial rings as in NGC 4314 (Benedict, Smith & Kenney 1996). So although we are only examining a single case, the failure of the hydrodynamic models to produce these morphologies in general is problematic.

Lastly, the models differ from the NGC 5383 observations because they produce a low density, ellipsoidal feature which encircles the bar region. The ellipsoid is present in the models throughout the simulation, and while its density varies, the density is always fairly low. This feature is not detected in our observations, and we are not aware of any barred galaxy with such a molecular gas feature; this may be due to the lack of sensitivity of current millimeter wavelength interferometers. The ellipsoidal feature probably correspond to the inner ring seen in optical images of other galaxies presented in the review by Buta & Combes (1996). The inner ring is usually a ring or ellipse of star formation which encircles the bar and may be associated with a 4:1 ultraharmonic resonance (Buta & Combes 1996). Good examples of this feature are seen in the continuum-subtracted H α images of NGC 3504 (Kenney et al. 1993) and NGC 6782, UGC 12646, IC 5240 (Crocker, Baugus & Buta 1996). Before we can discuss the importance and relevance of this feature to gas flows in bars, we would need to obtain additional observations of molecular gas emission and dust extinction to identify the feature, and we would need to study the models more carefully to establish the role of the gas in this ellipsoidal feature.

While there are many discrepancies between the model gas distribution and the observations, there are also some similarities. As already shown by A92, both straight and curved bar dust lanes are reproduced as a function of the bar strength by the hydrodynamic model. In our study, the model (Figure 6) predicts increasing gas density inwards in the dust lane; this matches the observations of CO emission and dust extinction (Figure 3, 5). A similar trend is also seen in the barred spiral NGC 1530 (See Figure 2.10 in Regan et al. 1995, or Figure 11 in Downes et al 1996).

In summary, the hydrodynamic model reproduces the observed offset dust lanes and the observed increase in gas density inwards along the dust lane. But there are key differences between the model and the observations. The model predicts a nuclear ring morphology with an extremely high density contrast between the ring and the dust lanes, whereas observations show a S-shaped morphology with three peaks with a relatively low density contrast between the dust lanes and the peaks.

4.3. Understanding the Differences between the Model and the Observations

4.3.1. *Is a Nuclear Bar Affecting the Observed Gas Density and Morphology?*

One reason for the absence of the predicted morphology could be the presence of a nuclear bar which could drive gas inwards from the twin peaks. We searched for a nuclear bar in a high resolution, high dynamic range NICMOS image (Figure 7a).

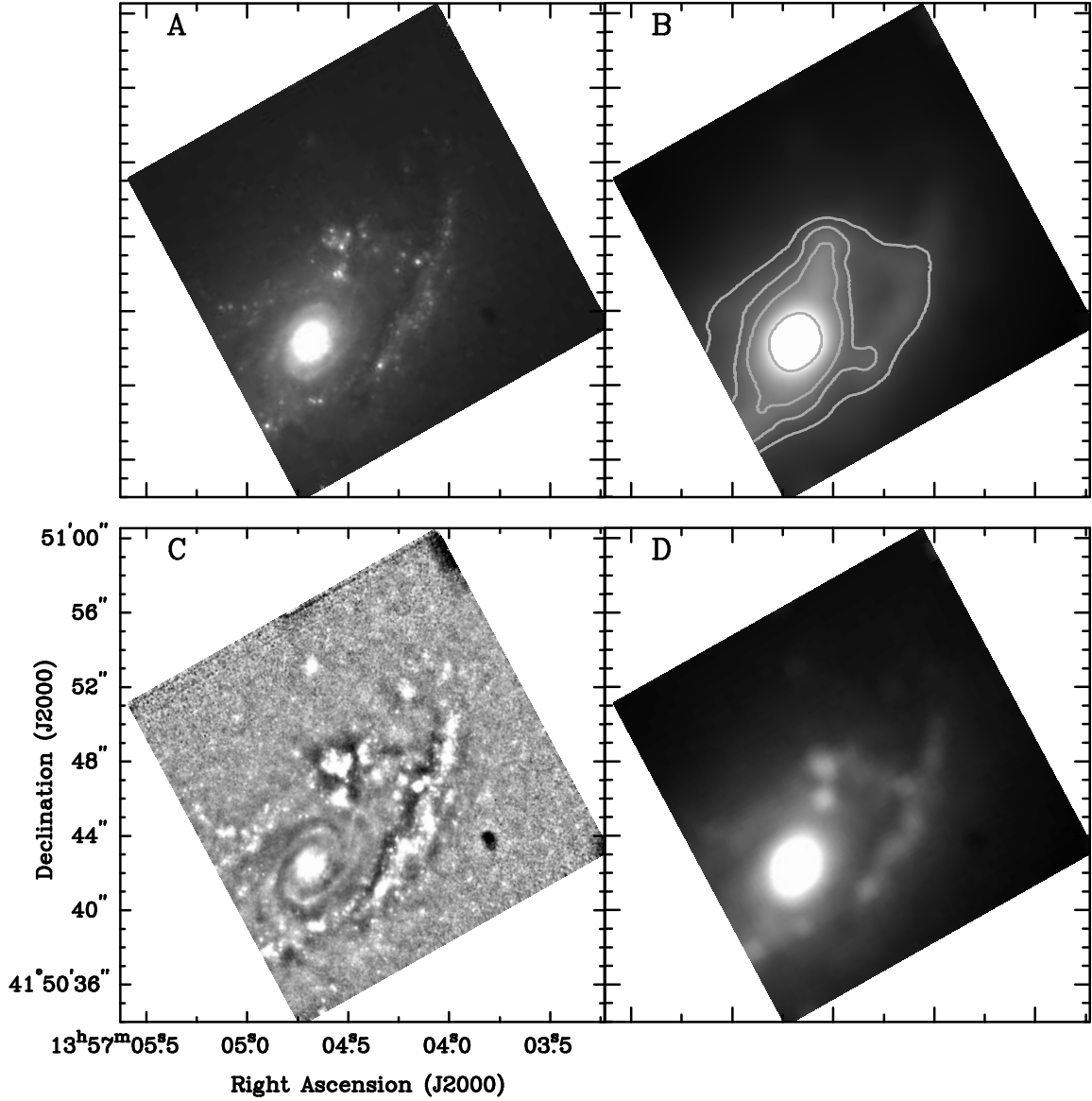


Fig. 7.— Top left: a) Original NICMOS image showing the nucleus and the northwestern dust lane in absorption. Top right: b) Same image as in panel (a) smoothed by a Gaussian with a FWHM of 14 pixels. Arbitrary contours are drawn on top of the image to show the fake “nuclear bar.” Bottom left: c) Unsharp masked image created by subtracting panel (b) from panel (a). The trailing spiral pattern is clearly seen all the way into an unresolved core. Bottom right: d) Same image as in panel (a) smoothed by a Gaussian with a FWHM of 7 pixels. Notice the fake “ring” around the nuclear bar.

The image shows a relatively smooth nucleus with a collection of star forming regions north northwest of the nucleus. These correspond to the peak HP seen in the lower resolution $H\alpha$ image

(Figure 1). The main bar dust lane can also be seen in absorption as it travels inwards towards the nucleus. There is no evidence of a nuclear bar at the center of NGC 5383.

Since the nucleus in NGC 5383 is quite bright, it is possible that weaker structure in this region may be difficult to discern. To investigate this possibility we applied the technique of unsharp masking where we subtracted a 14 pixel FWHM Gaussian smoothed image (Figure 7b) from the original image (Figure 7a). Pioneered by Malin & Zealey (1979), this technique allows one to distinguish weaker features from brighter ones by reducing the contribution of the bright background; however, we caution that the unsharp masking technique is not perfect and detailed studies of nuclear structure may benefit from multiple techniques. For our purposes the unsharp masking technique is adequate; the resulting image is shown in Figure 7. It shows a well-defined two arm, trailing spiral pattern which starts from the main northwestern dust lane and winds its way down to an unresolved core; there is no evidence of a nuclear bar. The observed trailing pattern is not unique to NGC 5383; central regions of other galaxies also show similar nuclear trailing spirals (e.g. NGC 3982, NGC 3032, Mkn 573 Regan & Mulchaey 1999 and references therein). This trailing spiral arm pattern may be a mechanism for transporting gas further inwards from the location of the inner Lindblad resonance (Regan & Mulchaey 1999) where the gas inflow is known to stall in modeling studies.

Models have not predicted this trailing spiral pattern. Analytic solutions predict a leading spiral structure inside the inner inner Lindblad resonance (IILR) (Combes 1996; Yuan & Kuo 1997). Although a trailing spiral pattern can be excited at the outer inner Lindblad resonance (OILR), only a leading spiral is excited by the IILR. It is unclear whether the OILR excited trailing spiral pattern can propagate inside the IILR. It is also unclear how the two spiral patterns interact and whether the relative amplitudes of the two patterns can appropriately account for these observations. These issues are under investigation (Yuan et al. 1999).

The smoothed image used for the unsharp masking (lower right hand corner in Figure 7) has a resolution and quality comparable to good ground-based images. In this image, we clearly see a nuclear bar-like feature at the center of NGC 5383 even though there is no bar in the original NICMOS image and in the unsharp masked image. The bar-like feature is created by the smoothing of the light from the bright star forming regions north and south of the nucleus which leads to the roughly north-south elongation, i.e. the fake bar. Smoothing the original image with a Gaussian with FWHM of 7 pixels, one can even create a partial circumnuclear ring (see Figure 7d). Although this is more difficult to see than the bar, an oval encircling the fake nuclear bar is clearly visible in this image. In reality, these structures are simply artifacts of the various smoothing techniques applied to the original image.

This result shows that study of the nuclear structures in a galaxy requires high resolution observations, and that ground-based images can be inadequate and worse, misleading in the identification of these structures. Another important point of note is that even in the H-band, where the effects of dust extinction and star formation are supposed to be minimized, these

NICMOS images clearly show star forming knots and dust features. The smoothing experiments show how these contaminants can create false features. So although near-infrared observations are desirable compared to optical observations (which are even more sensitive to these contaminants), the near-IR data also need to have high resolution to properly investigate nuclear features.

Thus, we conclude from this study of the NICMOS image of the center of NGC 5383 that a nuclear bar is not responsible for the differences between the observations and the model predictions.

4.3.2. Can the Hydrodynamic Model be Tuned to Account for the Morphology Discrepancies?

We considered the possibility that the hydrodynamic models could produce offset dust lanes without producing a nuclear ring. The motivation for this search came from an examination of the bi-modal outcomes (i.e. offset dust lanes with a ring versus centered dust lanes without a ring) of the previous studies by A92 and PST95. Since these studies took rather coarse steps in parameter space, we considered the possibility of an intermediate scenario where offset dust lanes could exist without a ring or with some other nuclear gas morphology. We studied the parameter space by varying three of the four free parameters in the PST95 model (the four parameters are the bar axial ratio, the central density, the Lagrangian radius or equivalently the pattern speed, and the quadrupole moment or equivalently the bar mass – see PST95 for details)¹⁸ in such a way as to encompass the transition region between the two outcomes described above. Though we found some new and interesting results from this experiment (see Appendix A), we did not find the intermediate scenario we were searching for; in every case where offset dust lanes formed, we found that a nuclear ring also formed (See Figure 9a,b,c) . Hence, we come to the conclusion that gas hydrodynamic processes alone cannot determine the nuclear region gas morphology.

4.3.3. Can Nuclear Star Formation Account for the Discrepancy?

Initial parameters and the length of time over which the bar has evolved both determine the density of the ring in the model. Since in the PST95 model the inflowing gas simply accretes in the nuclear ring over time, the density contrast between the ring and the dust lanes is destined to increase over time. The low density contrast in the observations of NGC 5383 might suggest that the bar in this galaxy is fairly young. However, similar low gas density contrast in several other barred spirals indicates that it is more likely that the gas is somehow being depleted from the ring. One way of depleting the gas would be to convert the gas into stars. Kenney et al. (1993) showed that in the nuclear region of NGC 3504, the Toomre Q parameter is close to its critical value; they suggested that the ongoing nuclear star formation could be explained using a simple gravitational

¹⁸We set the bar axial ratio to be 4 for our experiment

instability picture. Elmegreen (1994) also showed analytically that at typical nuclear ring radii ($r \sim 1$ kpc), star formation can occur via gravitational instability if the ring gas density is roughly $100 \times$ disk gas density (at $r \sim 10$ kpc), assuming that the disk gas density is nearly critical. In the models, the ring density is a factor of $50\text{--}200 \times$ initial disk density which is sufficiently high for star formation via gravitational collapse. Indeed, in the nuclear region in NGC 5383 (Figure 1), as in numerous other barred spirals (Phillips 1993; Garcia-Barreto et al. 1996), we observe vigorous, circumnuclear, massive star formation.

The nuclear star formation rate in NGC 5383 is at least $7 M_{\odot} \text{ yr}^{-1}$ (§4.4). If continuous star formation is assumed, this rate sets a lower limit on the mass inflow rate. Based on measurements in other barred spirals such as NGC 7479 and NGC 1530, which are similar to NGC 5383, it is likely that the mass inflow rate is lower (Quillen et al. 1995 and RVT97 measure inflow rates of $1\text{--}4 M_{\odot} \text{ yr}^{-1}$). But the mass inflow rate is a difficult quantity to measure and these numbers are highly uncertain. Still it is unlikely that the high nuclear star formation activity can be supported by a proportionally high mass inflow rate over an extended period of time (for example, an inflow rate of $10 M_{\odot} \text{ yr}^{-1}$, would deplete the total gas reserve ($10^{10} M_{\odot}$) of a typical galactic disk in only a billion years).

One can also compare the total gas mass in the center of NGC 5383 to the current star formation rate. Using the standard CO-H₂ conversion factor, the total molecular gas mass in the center of NGC 5383 is $2 \times 10^9 M_{\odot}$. Given that the dust and the CO intensities differ between the bar and the nuclear region, and given that the dust is probably a better tracer of the molecular gas mass, the total molecular gas mass calculated from the standard conversion factor is probably an upper limit to the total gas mass in the circumnuclear region. Therefore at the observed star formation rate of $7 M_{\odot} \text{ yr}^{-1}$, the gas reservoir at the center of NGC 5383 can be depleted in less than 3×10^8 yrs. So, as has been suggested before, circumnuclear star formation in NGC 5383 is probably an intense and episodic event (Shlosman 1992). Thus the observed low density contrast can be attributed to gas depletion via circumnuclear star formation. The simulations do not reproduce the observations because, although star formation can occur at the model densities, star formation is not modeled.

4.4. Star Formation Rate in NGC 5383

We used the H α luminosity to estimate the star formation rate in various regions in NGC 5383 (see Table 2). We measure an H α flux of $2.42 \pm 0.09 \times 10^{-12} \text{ ergs cm}^{-2} \text{ s}^{-1}$ in the central 3.5 kpc diameter region and a total H α flux in the galaxy of $4.37 \pm 0.36 \times 10^{-12} \text{ ergs cm}^{-2} \text{ s}^{-1}$. We converted the observed H α flux to a star formation rate using the empirical equation derived by Kennicutt (1983),

$$SFR(total) = \frac{L(H\alpha)}{1.12 \times 10^{41}} M_{\odot} \text{ yr}^{-1} \quad (1)$$

In deriving this equation Kennicutt assumed an average intrinsic dust extinction of 1.1 magnitudes in a galaxy. Since the dust extinction can vary dramatically in star forming regions (Phillips 1993), the exact optical depth is difficult to determine; hence, we use Kennicutt’s value to correct the observed fluxes for dust extinction. Using an adopted distance of 32.4 Mpc, we calculate the total star formation rate in NGC 5383 to be $12.6 M_{\odot} \text{ yr}^{-1}$, of which $7 M_{\odot} \text{ yr}^{-1}$, are formed in the nuclear region. For any single galaxy, this type of calculation of the star formation rate is uncertain by a factor of 2 (Kennicutt 1983). A previous calculation using a different technique and the $\text{H}\beta$ ionization line by Duval & Athanassoula (1983) resulted in a nuclear star formation rate of $8 M_{\odot} \text{ yr}^{-1}$; our results are consistent with their value. The star formation rate at the northeastern and southwestern bar ends is 1.9 & $3.2 M_{\odot} \text{ yr}^{-1}$, respectively, smaller than the star formation rate in the nuclear region.

The star formation rate of $7 M_{\odot} \text{ yr}^{-1}$, in the central 3.5 kpc of NGC 5383 is substantially higher than the average star formation rate over the entire disks of Sb and Sc type galaxies, which varies from 0.1 to $4 M_{\odot} \text{ yr}^{-1}$, (Kennicutt 1983). However, such a high star formation rate is not unusual for centers of barred spirals, and such activity is often classified as a starburst (e.g., Jogee 1999; Contini et al. 1997). The total mass of H_2 ($2 \times 10^9 M_{\odot}$) calculated earlier is also not unusual and it places NGC 5383 in company of galaxies such as NGC 4536 and NGC 2782 (Jogee 1999) which are both gas rich in the nuclear region and hosts to high nuclear star formation activity.

4.5. Star Formation in the Bar

Excluding the bar ends and the nuclear regions, early type barred spirals have very low star formation activity in the bar, even though the gas concentration is high in the bar dust lanes (Downes et al. 1996). As already shown in §4.2, the density contrast between the dust lanes and the center is small. Yet the star formation activity in the bar is limited compared to the center; several explanations have been put forth to account for this behavior. Tubbs (1982) suggested that

Table 2. Star Formation Rates in NGC 5383

Label	Name	Area (arcsec ²)	Flux (ergs cm ⁻² s ⁻¹)	SFR ($M_{\odot} \text{ yr}^{-1}$)
H-I	Nuclear region	1074	$2.42 \pm 0.085 \times 10^{-12}$	7
H-II	NE Bar end region	1026	$0.65 \pm 0.07 \times 10^{-12}$	1.9
H-III	SW Bar end region	1452	$1.09 \pm 0.11 \times 10^{-12}$	3.2
	The galaxy	4763	$4.37 \pm 0.36 \times 10^{-12}$	12.6

molecular clouds entering the dust lane could be dispersed due to their high velocities relative to dust lane gas. Athanassoula (1992) argued that the high shear in the bar dust lanes prevents star formation. RVT97 pointed to the large divergence in gas streamlines prior to the dust lanes, which they argued could tear apart molecular clouds or prevent their formation. Recently, Reynaud & Downes (1998) argued that a combination of the shear and shock in the dust lanes leads to the low star formation rate in the bar. These hypotheses argue effectively for the inhibition of star formation in the bar dust lanes. Yet some star formation does occur in the bar. Here we investigate precisely where and under what circumstances stars form in the bar.

The star formation sites can be traced by $H\alpha$ emission, whereas the molecular gas can be traced by either CO emission or dust extinction. The CO emission in the bar dust lanes of NGC 5383 is too weak to be detected, so we assume that the dust extinction traces the molecular gas (as suggested observations of NGC 1530 by Downes et al. 1996 and observations of NGC 3627 and NGC 2903 by RSV99). Figure 8 shows the overlay of the $H\alpha$ emission on the dust extinction in the bar on NGC 5383. Comparing the relative distribution of the star formation sites to the molecular gas distribution in this figure, one immediately notices two important features.

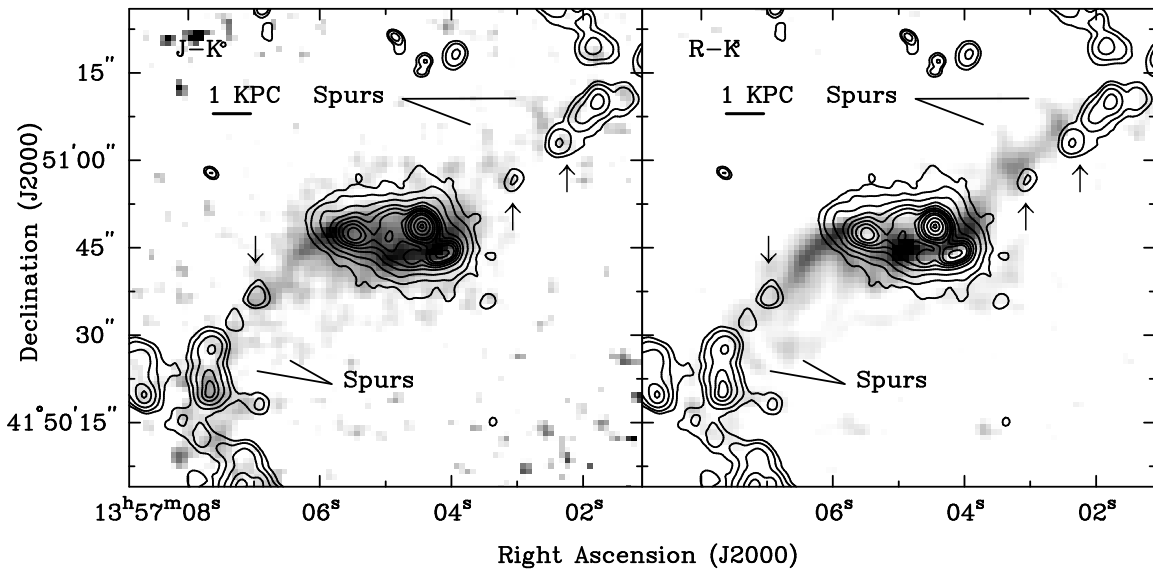


Fig. 8.— A plot of $H\alpha$ contours spaced at 15, 25, 50, 100, 150, 200, 250, 300, 400, 500, 700, 900, $1000 \times 5.6 \times 10^{-18}$ ergs $\text{cm}^{-2} \text{s}^{-1}$, overlaid on the J-K' (left panel) and R-K' (right panel) color maps. Note the location of the $H\alpha$ peaks, shown by the arrows, and the dust spurs. The $H\alpha$ peaks are all on the leading side of the dust lane directly across from the dust spurs.

First, the $H\alpha$ peaks are all located on the leading side of the bar dust lane. Second, these peaks occur preferentially near dust concentrations (see arrows in Figure 8); these $H\alpha$ peaks are found at the ends of dust spurs which are most clearly seen in the R-K' (Figure 5) image. The $H\alpha$ peaks and the dust peaks are roughly $\sim 3''$, or ~ 470 pc apart.

In order to place these observations in the context of the hydrodynamic model gas kinematics, we reiterate the predictions of the gas flow in the models. In these models, gas flows in elliptical streamlines until it encounters the main bar dust lane where the hydrodynamic shock redirects the gas inwards (RVT97; RSV99); *none* of the gas encountering the dust lane crosses the dust lane. Hence, the presence of $H\alpha$ emission on the leading side of the dust lane is surprising. This is because the recent massive star formation indicated by the $H\alpha$ emission is thought to occur only in areas of high gas concentration such as giant molecular clouds, or in larger complexes of such clouds called giant molecular associations (Blitz 1994 and references therein; Vogel, Kulkarni & Scoville 1988); the area on the leading side of the bar dust lane does not have high gas concentrations. Therefore, we conclude that these young stars must have formed elsewhere.

In the bar, the only regions suitable for star formation, i.e. regions of high gas concentrations, are the dust lanes and the dust spurs. The dust lane, however, is thought to be an inhospitable environment for various reasons already outlined above; the spurs are a plausible alternative. Since there is a one to one correspondence between the $H\alpha$ peaks and the dust spurs with the $H\alpha$ peaks located directly across from the spurs, it is likely that the spurs are involved in star formation. In context of the hydrodynamic gas flow, stars forming in the spurs would continue to move along their original elliptical orbits. These stars would pass ballistically through the dust lane, travel to the leading side and ionize the low density gas there. This would be consistent with the $H\alpha$ peaks being located directly across from the dust spurs. Another important reason for the spurs to be conducive to star formation is that, in addition to being regions of high gas density, the spurs are also located in a region of lower shear. Although we do not have a full velocity field map for NGC 5383 which shows the lower shear environment, the lower shear can be clearly seen in the gas, prior to its encounter with the dust lanes, in the maps of other barred galaxies such as NGC 1530 (RVT97).

The distance between the $H\alpha$ peaks and the dust concentrations at the end of the spurs puts a strong constraint on the velocity of the newly formed stars. If the stars form in the spurs, the stars must traverse ~ 500 pc in 10^7 years and therefore have velocities ~ 50 km s $^{-1}$ (in the rotating frame of the bar); indeed, velocities of this magnitude are present in the hydrodynamic model before the gas encounters the dust lane. So the distance between the $H\alpha$ peaks and the dust lanes is also consistent with star formation occurring in the spurs.

Thus we have addressed where and under what circumstances stars form in the bar, given the predictions of the hydrodynamic model gas flow. The observations presented here suggest the following scenario: at certain locations along the bar gas becomes highly concentrated and forms spurs. Star formation occurs in the spurs because of the high gas density *and* low shear. The newly formed stars move ballistically through the dust lane, ionizing the low density gas on the leading side of the bar and appearing directly across from the spurs, whereas the gas is redirected inwards down the dust lane.

However, one difficulty in applying this scenario to NGC 5383 is the lack of $H\alpha$ emission in

the spurs. The spurs are simply not dense enough to hide star formation and therefore one might expect to see $H\alpha$ emission from ongoing star formation in the spurs. The lack of such emission in NGC 5383 may be because we are observing very low levels star formation activity (2-3 peaks on each side) in the bar of this galaxy. Indeed, observations of other galaxies do show $H\alpha$ emission on both the leading and trailing sides of the bar dust lane (e.g., as in NGC 7479, Laine et al. 1999); however, it is not known whether this emission is associated with dust spurs. In any case, the one-to-one correspondence between the $H\alpha$ emission and the spurs in NGC 5383 is unlikely to be completely coincidental and therefore it is highly likely that the spurs are involved in the star formation activity.

Another interesting aspect of this scenario is that it points out the need for including gas self-gravity in the hydrodynamic model. The presence of the spurs clearly indicates that gas is becoming highly concentrated along the bar. In the region of the spurs, the divergent gas streamlines should prevent cloud formation (as pointed out by RVT97) but the presence of the spurs shows the importance of cloud self-gravity and cloud-cloud gravitational interactions. These effects are not modeled by the hydrodynamic simulations. So although these models are highly successful at reproducing the velocity fields and the straight dust lane morphology in bars, and they provide an adequate context for interpreting the observations of $H\alpha$ emission and the spurs in the bar, these models lack the self-consistency necessary to fully explain the star formation process.

5. Conclusions

The nuclear gas and dust distribution in the prototypical barred spiral NGC 5383 cannot be reproduced by the hydrodynamic models. Whereas the model always produces a high density contrast circumnuclear ring, the gas and dust are observed in a low density contrast S-shaped distribution. We have shown that the discrepancy cannot be eliminated by fine tuning the model.

The alternative possibility that a nuclear bar is responsible for the differences is eliminated by using a high resolution NICMOS image. Applying the unsharp masking technique, we find that the underlying nuclear structure is a trailing spiral pattern. We have also shown how coarser resolution data, such as that found in ground-based images, can lead to false identifications of nuclear bars and rings.

We conclude that the discrepancy between the observed and modeled gas distribution is due to the absence of star formation in the models; the vigorous $7 M_{\odot} \text{ yr}^{-1}$ circumnuclear star formation, which can deplete the gas and lead to the observed low density contrast, is not modeled by the hydrodynamic simulations.

Finally, we present an explanation for how stars may form in the bar between the bar ends and the circumnuclear region. In our scenario, stars form in dust spurs before the gas encounters the dust lane. The spurs, unlike the high shear/high density dust lane, are more conducive to star

formation because they are regions of low shear and high density. Stars which form in the spurs travel ballistically through the hydrodynamic shock at the dust lane, ionizing the low density gas on the leading side of the dust lane, whereas the gas is redirected down the dust lane. Thus, HII regions can even be found on the leading side of the main bar dust lanes.

We thank the referee, Jeff Kenney for his careful reading of the original manuscript and his numerous useful suggestions which have resulted in a far superior paper. We would also like to thank Lee Armus for obtaining the optical images and Eve Ostriker for helpful discussions and suggestions which resulted in Figure 10. We thank Jim Stone for providing the hydrodynamic model code and for his invaluable insights in interpreting the models. K.S would like to thank M. Thornley, L. Looney, M. Wright, J. Morgan and R. Forster for their help with BIMA data acquisition and reduction. K.S. would also like to acknowledge useful discussions with S. Veilleux, Y. Fernandez, A. Koratkar, N. Volgenau and J. Crawford. This research was supported by NSF grant AST 9314847 and AST 9613716.

6. Appendix A

Previous hydrodynamic models of gas flow in a barred potential have resulted in one of two outcomes: either offset dust lanes and a nuclear ring form or centered dust lanes without a ring form. In this section we describe our experiment intended to find an intermediate case where offset dust lanes could form without the formation of a nuclear ring? To that end, we have explored the parameter space using the PST95 model near the transition region using finer steps than those used by A92 and PST95.

The PST95 hydrodynamic models are computed with a third-order piecewise, parabolic method (PPM) with a cylindrical coordinate system yielding a resolution of 8 pc at a distance of 0.1 kpc. The gravitational potential used in this model consists of a Kuzmin-Toomre disk, a bulge and a bar described by a Ferrer’s ellipsoid. The model is completely determined by four independent input parameters: the bar axial ratio (a/b), the central density (ρ_c , $10^6 M_\odot \text{kpc}^{-3}$), the Lagrangian radius (r_l , kpc, equivalently the pattern speed), and the quadrupole moment (q_m , $10^6 M_\odot \text{kpc}^2$, equivalently the bar mass) (see PST95 for details). We chose to set $a/b = 4.0$ and varied the other three parameters as follows: $1.0e4 < \rho_c < 7.4e4$, $5.0 < r_l < 7.5$, $1.5e4 < q_m < 7.5e4$. Since any of these three free parameters can affect the transition between the two outcomes of the model, we varied one parameter at a time while setting the other two parameters to the “standard” model values used by PST95. As in PST95, we ran each simulation until the bar had settled into a quasi-static state i.e. until $t = 2.0$ Gyr (see PST95 for more details on time evolution of the bar). The final azimuthally averaged log density versus radius are plotted in Figure 9.

We find that the formation of the ring is indeed abrupt in all instances where an ILR exists. In other words, if offset dust lanes form, a nuclear ring inevitably forms. With this result, we

Table 3. Parameters for models which produced rings

Model #	r_l (kpc)	q_m ($10^{10} M_\odot$ kpc ²)	ρ_c ($10^{10} M_\odot$ kpc ⁻³)
1	5.85	4.5e4	2.4e4
2	5.90	4.5e4	2.4e4
3	5.95	4.5e4	2.4e4
4	6.00	4.5e4	2.4e4
5	6.25	4.5e4	2.4e4
6	6.50	4.5e4	2.4e4
7	6.75	4.5e4	2.4e4
8	7.0	4.5e4	2.4e4
9	7.5	4.5e4	2.4e4
10	6.0	1.5e4	2.4e4
11	6.0	2.5e4	2.4e4
12	6.0	3.5e4	2.4e4
13	6.0	4.0e4	2.4e4
14	6.0	4.7e4	2.4e4
15	6.0	4.5e4	2.3e4
16	6.0	4.5e4	2.6e4
17	6.0	4.5e4	2.8e4
18	6.0	4.5e4	3.0e4
19	6.0	4.5e4	3.7e4
20	6.0	4.5e4	4.0e4
21	6.0	4.5e4	7.4e4

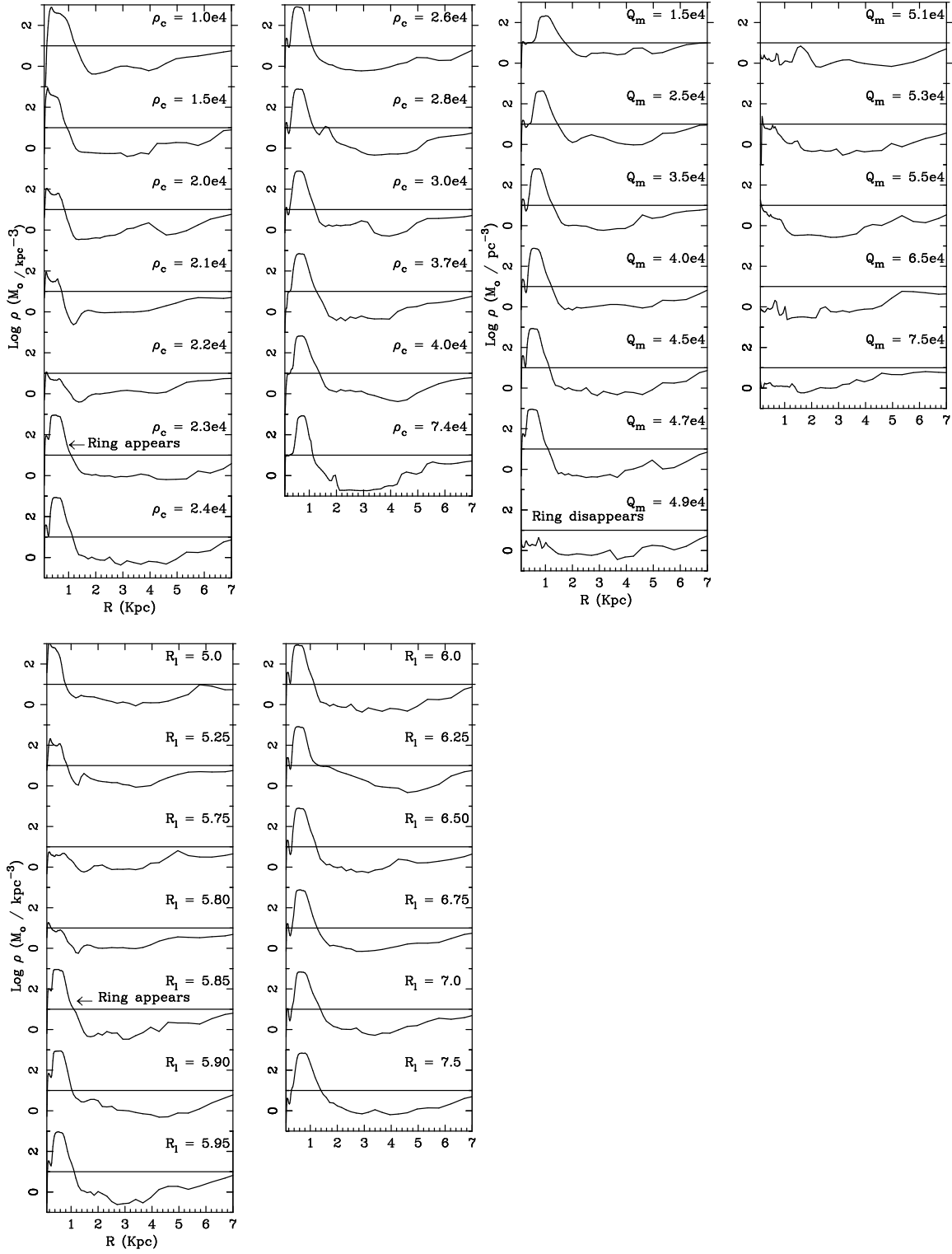


Fig. 9.— Azimuthally averaged log density versus radius for different hydrodynamic models. The horizontal line is the initial density. The standard parameters are $a/b=4.0$, $\rho_c = 2.4e4 \times 10^6 M_\odot \text{kpc}^{-3}$, $Q_m=4.5e4 \times 10^6 M_\odot \text{kpc}^2$, $r_l=6.0 \text{ kpc}$. When one of the three free parameters is varied (as indicated on the individual plots), the others are set to these standard values.

conclude that the intermediate case, if present, exists in even finer steps of the model parameters; otherwise we confirm PST95’s assertions about the robustness of the nuclear ring. Although this experiment failed in finding the intermediate scenario which may have explained the observations of NGC 5383, we discovered other interesting results which add to our current understanding of gas distribution in the hydrodynamic models.

First, when the ring exists, we find that the ring seems to be located at approximately the same distance and has approximately the same thickness growing only slightly thinner with higher central density concentration. Since the commonly accepted explanation for the location of the nuclear ring is that it must exist between the outer ILR (OILR) and the inner ILR (IILR), one can conclude that the ring location and thickness should be restricted to a certain range of radii. We find that in all 21 model runs (Table 3) which produce a ring, the ring peak is always located between the OILR and the IILR as shown in Figure 10.

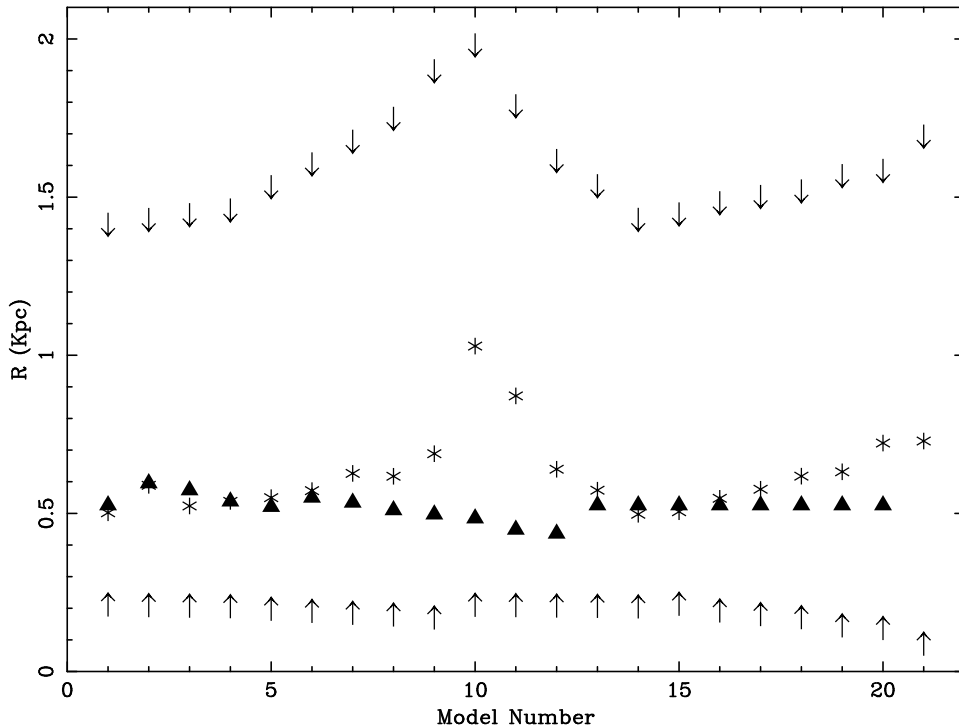


Fig. 10.— A plot of the Lindblad numbers: OILR (down arrow), IILR (up arrow), maximum (triangle) of the Ω - $\kappa/2$ curve and the ring peak (star) for different models (Table 3) is shown. The ring peak always lies between the OILR and the IILR. Its location is not coincident with the maximum of the Ω - $\kappa/2$ curve but seems to be determined by the location of the OILR.

Interestingly, we also find that the location of the ring peak does not coincide with the location of the Ω - $\kappa/2$ maximum (Figure 10) as suggested by PST95 except for the standard model. In most cases the ring peak is close to the maximum of the Ω - $\kappa/2$ curve, but its location seems to be determined by the location of the OILR for a given model. In other words the location of the

ring peak and the OILR varies in exactly the same way for the different models but by different amounts from model to model. While this relationship is interesting, we note that it may not be physical since the OILR is located at a large distance ($\sim 1.5\text{-}2$ kpc) from the center; at these distance, the gas is no longer on circular orbits and hence the classical definition of an OILR may not be relevant. It would be, perhaps, more interesting to compare the location of the ring peak to the x1 and x2 orbits in the various models.

REFERENCES

- Athanassoula, E. 1992, MNRAS, 259, 328
- Athanassoula, E. 1992, MNRAS, 259, 345
- Becker, R. H., White, R. L., & Helfand, D. J. 1995, ApJ, 450, 559
- Benedict, F.G., Smith, B.J., & Kenney, J.D.P. 1996, AJ, 111, 1861
- Blitz, L. 1993, Protostars and Planets III, eds. E.H. Levy & J.I. Lunine (Tucson:Univ. of Arizona Press), 12
- Burbidge, E.M., Burbidge, G.R., & Prendergast, K.H. 1962, ApJ., 136, 704
- Buta, R. & Combes, F. 1996, Fundamentals of Cosmic Physics, 17, 95
- Combes, F., & Gerin, M. 1985, A&A, 150, 327
- Combes, F. 1996, in IAU Colloquium 157, Barred Galaxies, eds. R. Buta, D.A. Crocker, & B.G. Elmegreen, (San Fransisco:ASP), 286
- Contini, T., Wozniak, H., Considere, S., Davoust, E. 1997, A&A, 324, 41
- Downes, D., Reynaud, D., Solomon, P., & Radford, S.J.E. 1996, ApJ, 461, 186
- Duval, M. F. & Athanassoula, E. 1983, A&A, 121, 297
- Elmegreen, B. G. 1994, ApJ, 425, L73
- Elmegreen, B. G., & Elmegreen, D. B. 1985, ApJ., 288, 438
- Elmegreen, B.G. & Block, D. L. 1999, MNRAS, 303, 133
- Garcia-Barreto, J.A., & Carrillo, R., Venegas, S. & Escalante-Ramirez, B. 1996, in IAU Colloquium 157, Barred Galaxies, eds. R. Buta, D.A. Crocker, & B.G. Elmegreen, (San Fransisco:ASP), 76
- Heller, C. H., & Shlosman, I. 1994, ApJ, 424, 84
- Ho, L.C., Fillipenko, A.V., & Sargent, W. L. W. 1997, ApJ, 487, 591
- Hogböm, J.A. 1974, A&AS, 15, 417
- Huntley, J.M. 1978, ApJ, 225, 101
- Jogee, S. 1999, Ph. D. Thesis, Yale University
- Kenney, J. D. P., & Lord, S. D. 1991, ApJ, 381, 118
- Kenney, J. D. P., Wilson, C. D., Scoville, N. Z., Devereux, N. A., Young, J. S. 1992, ApJ, 395, L79
- Kenney, J.D.P., Carlstrom, J.E., Young, J.S. 1993, ApJ, 418, 687
- Kenney, J. D. P. 1996, in IAU Colloquium 157, Barred Galaxies, eds. R. Buta, D. A. Crocker, & B. G. Elmegreen, (San Fransisco:ASP), 150
- Kennicutt, R.C. 1983, ApJ, 272, 54

- Koopmann, R.A., & Kenney, J.D.P. 1996, in IAU Colloquium 157, Barred Galaxies, eds. R. Buta, D.A. Crocker, & B.G. Elmegreen, (San Fransisco:ASP), 105
- Laine, S., Kenney, J.D.P., Yun, M.S., Gottesman, S.T. 1999, ApJ, 511, 709
- Malin, D. F., & Zealey, W.J. 1979, Sky & Telescope, 57, 354
- Marco, O., & Alloin, D. 1998, A&A, 336, 823
- Martin, P., & Roy, J. 1994, ApJ, 424, 599
- Martinet, L., & Friedli, D. 1997, A&A, 323, 363
- Mulchaey, J.S., Regan, M.W., & Kundu, A. 1997, ApJS, 110, 299
- Norman, C. A., Sellwood, J. A., & Hasan, H. 1996, ApJ, 462, 114
- Ohta, K., Sasaki, M., Saito, M. 1986, PASJ, 38, 677
- Oke, J. B., & Gunn, J.E. 1983, ApJ, 266, 713
- Peterson, C.J., Rubin, V.C., Ford, W. K., Thonnard, N. 1978, ApJ, 219, 31
- Phillips, A.C. 1993, Ph.D. Thesis, University of Washington
- Piner, B.G., Stone, J.M., Teuben, P.J. 1995, ApJ, 449, 508
- Quillen, A.C., Frogel, J.A., Kenney, J.D.P., Pogge, R.W., Depoy, D.L. 1995, ApJ, 441, 549
- Regan, M.W., Vogel, S.N., & Teuben, P.J. 1995, ApJ, 449, 576
- Regan, M. W., Vogel, S.N., Teuben, P.J. 1997, ApJ, 482, 135
- Regan, M.W., & Mulchaey, J. 1999, AJ, 117, 2676
- Regan, M.W., Sheth, K., & Vogel, S.N. 1999, ApJ, in press
- Regan, M.W. 2000, ApJ, in preparation
- Reynaud, D., & Downes, D. 1998, A&A, 337, 671
- Sandage, A. & Bedke, J. 1994, The Carnegie Atlas of Galaxies, (Publ. 638; Washington D.C., Carnegie Institution of Washington)
- Sancisi R., Allen R. J., Sullivan III, W. T. 1979, A&A, 78, 217
- Sellwood, J. A., & Wilkinson, A. 1993, Rep. Prog. Phys, 56, 173
- Sellwood, J. A., & Moore, E. M. 1999, ApJ, 510, 125
- Sakamoto, K., Okumura, S. K., Ishizuki, S., Scoville, N. Z. 1999, ApJ, in press
- Shlosman, I. 1992, in Relationship Between Active Galactic Nuclei and Starburst Galaxies, ed. A. V. Filippenko, (San Fransisco:ASP), 335
- Sodroski, T. J. et al. 1995, ApJ, 452, 262
- Teuben, P. J. 1996, in IAU Colloquium 157, Barred Galaxies, eds. R. Buta, D.A. Crocker, & B.G. Elmegreen, (San Fransisco:ASP), 299

- Thatte, N., Quirrenbach, A., Genzel, R., Maiolino, R., & Tecza, M. 1997, *ApJ*, 490, 238
- Thompson, A.R., Moran, J.M, & Swenson, G.W. 1986, in *Interferometry and Synthesis in Radio Astronomy* (John Wiley & Sons)
- Tremaine S., & Weinberg, M.D. 1984, *MNRAS*, 209, 729
- Tubbs, A.D. 1982, *ApJ*, 255, 458
- Vogel, S.N., Kulkarni, S.R., & Scoville, N.Z. 1988, *Nature*, 402
- Wainscoat, R.J., & Cowie, L.L. 1992, *AJ*, 103, 332
- Weinberg, M.D. 1985, *MNRAS*, 213, 451
- Witt, A.D., Thronson, H.A., & Capuano, J.M. 1992, *ApJ*, 393, 611
- Yuan, C., & Kuo, C. 1997, *ApJ*, 486, 750
- Yuan, C., Sheth, K., Regan, M.W., & Vogel, S.N. 1999, in preparation